Numerical Simulation of Electromagnetic Flow Control for Hypersonic Systems

Jonathan Poggie*

Computational Sciences Center
United States Air Force Research Laboratory

ABSTRACT

The prospects for electromagnetic flow control for hypersonic systems were examined using computational tools developed to model ionized compressible flows. A careful analysis of experiments on shock propagation through a glow discharge showed that a nonuniform upstream temperature field is probably the primary cause of changes in the behavior of the shock. Magnetic control of reentry flows was also examined, and a significant reduction in stagnation point heat transfer was observed with the application of magnetic deceleration. Preliminary calculations of the interaction of plasma sheaths with a supersonic crossflow were made, with potential application to local flow control. Finally, the magnetohydrodynamic bypass concept for scramjet engines was explored, and promising results were obtained for a simplified three-dimensional scramjet configuration.

INTRODUCTION

Electromagnetic control of hypersonic flow was first considered in the late 1950s in conjunction with the atmospheric reentry problem [1,2], and more recent interest has been motivated to a large extent by the Russian AJAX vehicle concept [3]. Over the past few years, the Air Force Research Laboratory Computational Sciences Center has been developing a set of computational tools to study possible electromagnetic flow control techniques [4–16]. A fully three-dimensional magnetohydrodynamic code suitable for computations at both relatively high and low magnetic Reynolds numbers has been developed. In addition, a prototype two-dimensional code has been written in which the assumption of quasi-neutrality is relaxed in order to examine the plasma sheaths present on electrode surfaces.

In the present paper, we present a critical review of plasma technologies based on our recent computational studies, and provide an outlook for future research in the field of electromagnetic flow control. The plasma-based control technologies considered include manipulation of the bow shock through ionization upstream, the magnetohydrodynamic bypass concept, magnetohydrodynamic deceleration for stagnation point heat transfer mitigation, and local manipulation of the near-wall region in supersonic flow.

Motivation for work on plasma-based manipulation of the bow shock on a transatmospheric vehicle comes

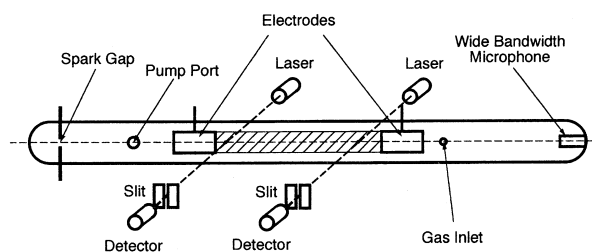*Address: AFRL/VAAC, 2210 EIGHTH ST, WPAFB OH 45433-7512, USA. Email: Jonathan.Poggie@wpafb.af.mil

Fig. 1   Schematic diagram of experiments in glow discharge tube. From Ganguly *et al.* [18], used with permission.

from experimental studies which have reported changes in the speed, strength, and structure of shock waves with the introduction of nonequilibrium ionization upstream [17,18]. There is, however, an ongoing controversy over the interpretation of the phenomena observed in the experiments. This issue will be discussed in the section 'Shockwave Control.'

Some of the most promising applications of magnetohydrodynamic control lie in mitigating the extreme heating that occurs in hypersonic flight. One application, termed the 'magnetohydrodynamic bypass,' involves energy extraction to reduce temperature and velocity in scramjet engine inlets, with a corresponding acceleration at the outlet (discussed under 'Magnetohydrodynamic Bypass,' below). Another application uses external flow deceleration to reduce local heating on a vehicle surface in extremely high speed flight, as in atmospheric entry. This control scheme will be examined in the section 'Heat Transfer Mitigation.'

Except at the extremely high Mach numbers of reentry flight, the level of electrical conductivity provided 'naturally' by thermal ionization is relatively small. The corresponding penalty in weight and power consumption for augmenting the electrical conductivity on a large scale could be quite high, and the most practical applications in this regime will probably be for local flow control, such as the stabilization of unsteady separation or control of boundary layer transition. A preliminary analysis of the influence of plasma sheaths in local control will be presented in the section 'Sheaths.'

SHOCKWAVE CONTROL

Over the last few years, the hypersonics research community has been exploring the possibility of improving transatmospheric vehicle performance by introducing weak nonequilibrium ionization upstream of the bow shock. Interest has been motivated in part by the ex-
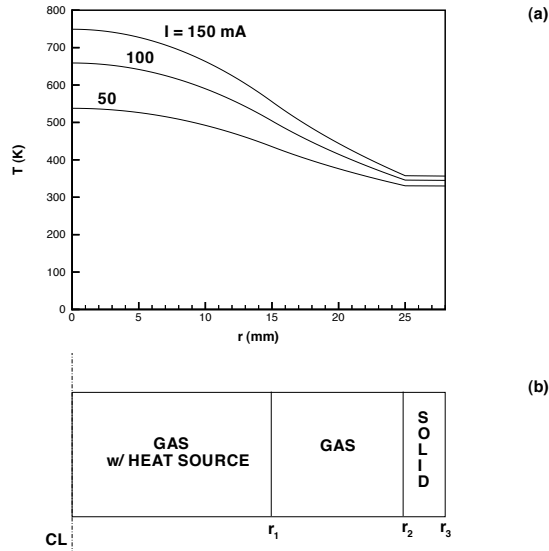
Fig. 2 Analytical heating model. Dimensions: $r_1 = 15$ mm, $r_2 = 25$ mm, $r_3 = 28$ mm. (a) Temperature profiles. (b) Diagram.

periments of Klimov *et al.* [17], in which a shock was generated with a spark discharge and propagated down a tube through an ionized region. An increase in the speed and a decrease in the strength of the shock were observed with the presence of weak ionization upstream. Ganguly *et al.* have replicated and extended this work more recently in a well-documented set of experiments [18]. Early studies by Voinovich *et al.* [19] and Hilbun [20] pointed out the possibility that the effects observed in these experiments were primarily due to temperature variations upstream of the shock, rather than effects inherent to ionization. We examined this issue in detail by carrying out careful simulations [4,6,7] of the experiments of Ganguly *et al.* These computations will be described in this section.

A schematic diagram of the apparatus for the experiments carried out by Ganguly *et al.* is shown in Fig. 1. The tests were carried out in a 50 mm diameter Pyrex tube, which was roughly 1 m long and was filled with argon gas. The pressure was fixed at about 4.0 kPa (30 torr) using a regulated purge flow. A shock was generated at the spark gap with an energy release of about 100 J. Downstream of the spark gap, a pair of 30 mm diameter cylindrical electrodes, separated by 300 mm, were used to generate a longitudinal plasma, with the cathode on the left in the diagram. The arrival of the shock pulse was recorded using a laser deflection technique at two stations located in the positive column of the glow discharge.

Since direct measurements of the initial temperature field were not made by Ganguly *et al.*, an analytical model was developed to predict the temperature field in the glow discharge as a function of the applied current. A conceptual diagram of a cross-section of the discharge is given in Fig. 2b. The model considered both the gas and the solid Pyrex wall of the tube; the discharge region was assumed to be heated by a uniform source term representing Joule heating by the discharge current. The
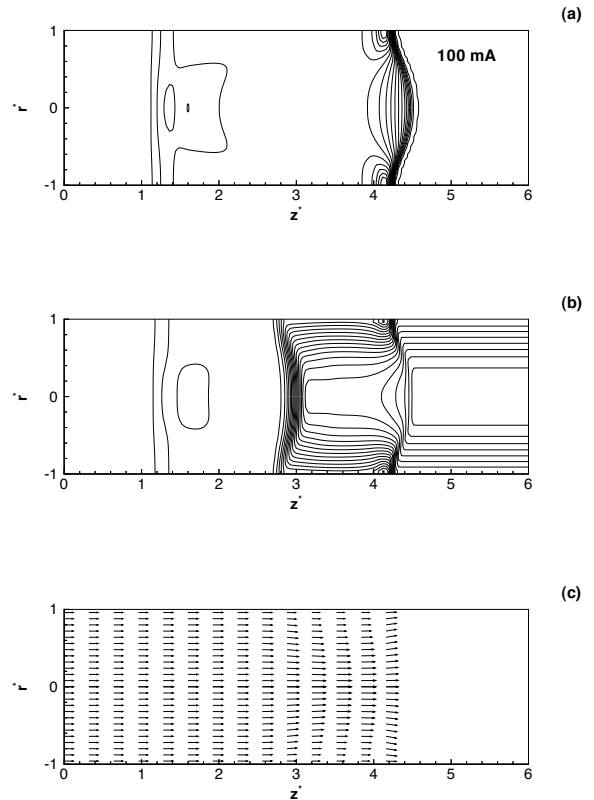

Fig. 3 Flowfield for $I = 100$ mA in 4 kPa argon at $t^* = 2$. (a) Pressure. (b) Density. (c) Velocity vectors.

model assumed that there was no gas flow inside the tube before the passage of the shock, and a one-dimensional heat conduction equation was solved in cylindrical coordinates. A symmetry boundary condition was imposed at the centerline and a convection model was imposed at the outer boundary. Expressions for the resulting temperature profiles are provided in Ref. [6]. Figure 2a shows example temperature profiles for three values of the discharge current. The scale of the abscissa matches the schematic diagram in Fig. 2b.

The temperature field predicted by this analytical model was used as input to two fluid dynamic models based on the Euler equations. The first model considered only the effect of thermal non-uniformity in the axial direction, replacing the radial temperature profile with a representative temperature. The interaction of the shock and the heated region was modeled as a plane shock impinging at normal incidence on a plane contact surface. The problem was solved by numerical solution of the algebraic equations of Ford and Glass [21].

The second model examined the problem using the Euler equations in an axisymmetric geometry. The computational domain was a $22.5°$ wedge-shaped region, six tube radii long, extending from the axis of symmetry to the inner wall of the tube. Uniform grid spacing was used along each coordinate, and the computations were carried out on a grid of $26 \times 5 \times 151$ points along the radial, circumferential, and axial directions, respectively.

Figure 3 shows the basic features of the flow for the 100 mA case at $t^* = 2$. The Mach number of the inci-
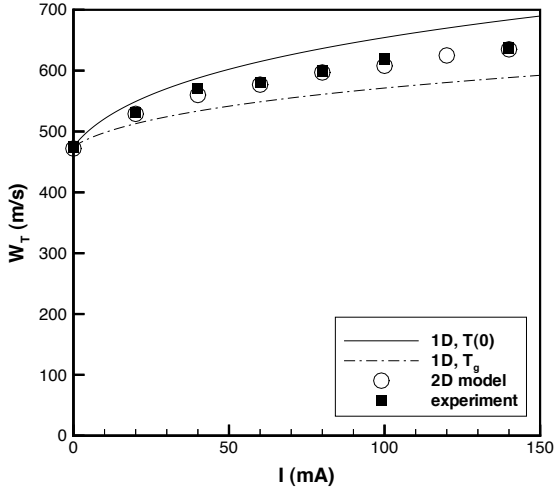
**Fig. 4   Transmitted shock speed as a function of discharge current in argon at 4.0 kPa (30 torr).**

Fig. 5   Shock signature in photodetector signal, $I = 100$ mA in argon at 4 kPa. (a) Density field, $t^* = 2$. (b) Directional derivative along axis, averaged along radius, $z^* = 3$.

dent shock was taken to be $M_I = 1.47$, determined from the experimental average shock speed between the two photodetector stations for the case with no plasma. The pressure, density, and velocity vector fields are shown, respectively, in parts (a)-(c) of the figure. The transmitted shock wave is evident as a bowed interface in the vicinity of $z^* \approx 4.4$. The shock is strongest in the vicinity of the wall, where local maxima appear in the pressure and density fields. Note that these maxima do not indicate flow separation; there is no recirculation present in the flowfield.

The average shock-pulse velocity between the two photodetector stations was chosen as an unambiguous parameter for comparison to the theoretical models. The arrival time at each of the two stations was determined by the first rise above the ambient signal level discernible by eye in the time-series plots in Ganguly *et al.* The average velocity of the shock pulse between the two stations was determined by dividing the distance between stations (120 mm) by the difference in arrival time.

Figure 4 shows the shock speed predicted for different current levels by the one-dimensional and two-dimensional fluid models, combined with the gas heating model. Since the discharge temperature varies in the radial direction, a representative temperature must be selected for use in the one-dimensional fluid model, which neglects variation in that direction. The lines indicate the predictions of the one-dimensional model for two choices of the temperature on the right of the contact surface: the centerline temperature (solid line) and the average gas temperature (dash-dot line). The open symbols indicate values derived from the axisymmetric computation using the full temperature profile from the heating model. The one-dimensional model is seen to provide a fair estimate of the trend predicted by the more realistic axisymmetric model; the predictions for the two choices of the temperature of the heated gas bracket the results from the axisymmetric computations.

The experimental average shock speeds are indicated by filled, square symbols in Fig. 4. The shock speed is
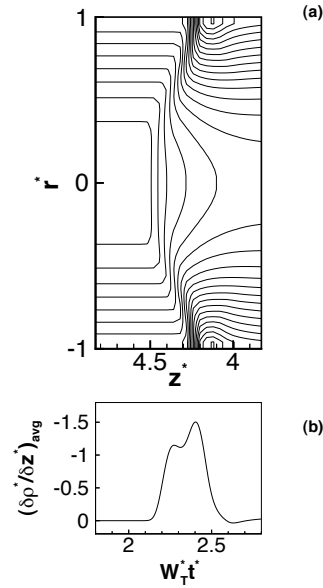
seen to rise from an initial value of about 470 m/s with no current flowing to about 640 m/s at $I = 140$ mA. The predictions from the combination of the temperature profile from the heating model and the axisymmetric, inviscid-flow computation are seen to agree with the experiments within the scatter in the experimental data, and within the uncertainty in determining the shock speed from the computed flow field.

One interesting observation in the spark-tube experiments was the appearance of multiple peaks in the photodetector signal when the plasma was present. These peaks have been attributed to a splitting or dispersion of the shock [18]. A numerical simulation of the photodetector signal was carried out to investigate this phenomenon.

As the laser beam passes through the experimental apparatus, it is deflected by changes in the index of refraction brought about by density variations. The slits in front of the photodetectors cut out a portion of the deflected beam, so that the amount of light reaching the photodetectors is a function of the beam deflection. The signal recorded by the photodetectors corresponds to the derivative of density along the direction normal to the slits (i.e., along the axis of the tube), averaged over the optical path.

Figure 5b shows a simulated laser deflectometer signal: the average across the radius of the directional derivative $\partial \rho^* / \partial z^*$ plotted against an effective distance $W_T^* t^*$. For comparison, Fig. 5a shows a portion of the density field; the z-axis has been flipped to correspond to the lower plot. The bowed shock is seen to produce a double-peak signal, as seen in the experiments.

Since the original publication of our computations, a thorough experimental and computational study of the glow discharge shock propagation problem has been published by Macheret *et al.* [22]. In this work, ultraviolet

filtered Rayleigh scattering was used to obtain point measurements of the temperature in the glow discharge. The measured temperature profiles were used as input to an axisymmetric, inviscid-flow computation. Excellent agreement was obtained between experiment and theory in measures of shock velocity and shock distortion as a function of discharge current. This paper sets an extremely high standard for future work: to prove a non-thermal effect on shock structure, studies will have to provide a comparable level of detail in documenting the effect of thermal nonuniformity.

HEAT TRANSFER MITIGATION

To examine the possibility of heat transfer mitigation through magnetic deceleration, magnetohydrodynamic computations were carried out in the low magnetic Reynolds number regime [8,10,16]. In this formulation, the conservation of mass, momentum, and energy is expressed as:

$$\frac{\partial \rho}{\partial t} + \nabla \cdot (\rho \mathbf{u}) = 0, \tag{1}$$

$$\frac{\partial}{\partial t}(\rho \mathbf{u}) + \nabla \cdot (\rho \mathbf{u}\mathbf{u} - \mathbf{\Sigma}) = \mathbf{j} \times \mathbf{B}, \tag{2}$$

$$\frac{\partial \mathcal{E}}{\partial t} + \nabla \cdot (\mathbf{u}\mathcal{E} - \mathbf{\Sigma} \cdot \mathbf{u} + \mathbf{Q}) = \mathbf{E} \cdot \mathbf{j}, \tag{3}$$

where $\mathcal{E} = \rho(\epsilon + u^2/2)$ is the total fluid energy per unit mass, $\Sigma_{ij} = -p\delta_{ij} + \tau_{ij}$ is the total stress tensor, and $\mathbf{Q}$ is the heat flux. The current was determined from Ohm's law:

$$\mathbf{j} = \sigma \cdot [\mathbf{E} + \mathbf{u} \times \mathbf{B}], \tag{4}$$

with a scalar electrical conductivity. Since the Hall effect has been neglected, it can be shown [23] that axial symmetry requires that $\mathbf{E} = 0$. The magnetic field was taken to be a dipole centered at the origin.

The case of a Mach 5, ideal gas flow over a hemisphere was chosen to match the inviscid computations of Coakley and Porter [24]. The results were compared to these early computations and to the inviscid theory of Bush [23] (with $\mathrm{Re}_m = 0$). Additional viscous calculations were carried out to examine the influence of magnetic control on the heat transfer in the vicinity of the stagnation point, and were compared to Bush's boundary layer theory [25].

The freestream conditions were $M = 5$ and $\gamma = 1.4$. The inviscid computations were carried out on an axisymmetric grid of $60 \times 40 \times 5$ points distributed, respectively, in the directions along the body surface, normal to the body, and in the circumferential direction.

The basic flow structure is illustrated in Fig. 6, which shows the pressure field predicted by the numerical computations for two cases: $Q = 0$ and $Q = 6$, where $Q = \sigma B_0^2 R/\rho_\infty V_\infty$ is the magnetic interaction parameter. With the application of a strong magnetic field, there is a dramatic increase in the shock standoff, but little qualitative change in the flow structure.

The increase in shock standoff with interaction parameter is quantified in Fig. 7. The predictions of Bush's theory [23], Coakley and Porter's computations [24], and
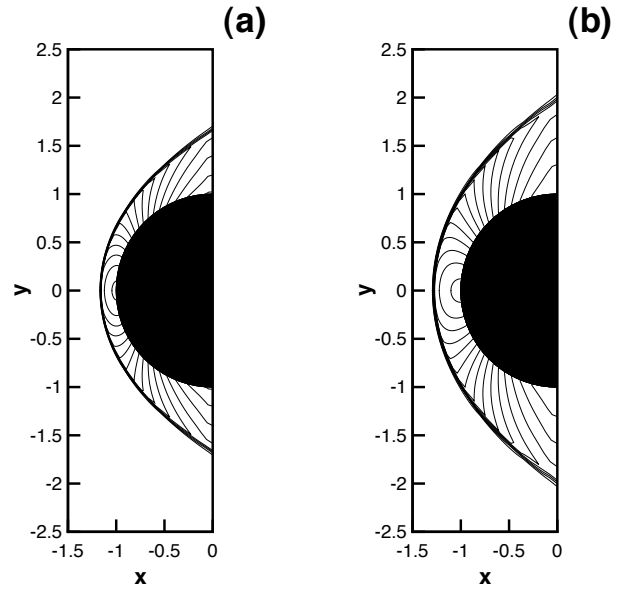

Fig. 6 Pressure field p/p_∞ for inviscid flow (contour interval 2). (a) $Q = 0$ (b) $Q = 6$
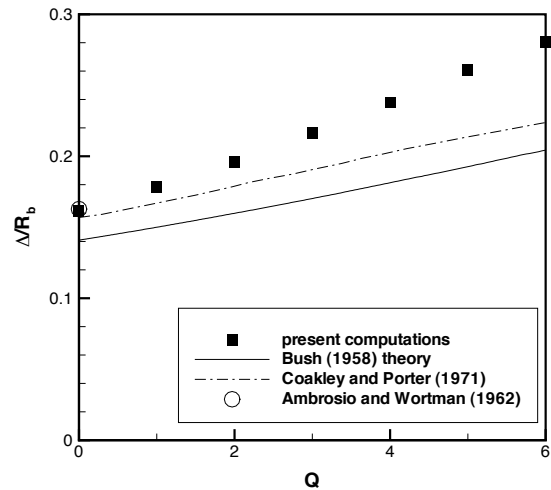

Fig. 7 Effect of applied magnetic field on shock standoff ($M = 5$, $\gamma = 1.4$).

the correlation of Ambrosio and Wortman [26] are shown for comparison with the results of the present computations. As expected for a constant-density calculation, the prediction of the Bush theory tends to be too low for the non-magnetic case, whereas the results from Coakley and Porter and the present computations are close to the empirical correlation. Although all methods predict higher standoff with increasing interaction parameter, the present computations show a more rapid rise.

A corresponding set of viscous computations was carried out for Mach 5 flow with $\gamma = 1.4$ and $\mathrm{Re} = 80000$. Two grids were used: a baseline case with $60 \times 80 \times 5$ points, and a finer grid of $120 \times 160 \times 5$ points. Figure 8 shows boundary layer profiles of velocity and temperature for a station close to the centerline. The circular and square symbols show, respectively, the results from the coarse and fine grid computations. The solid lines in-
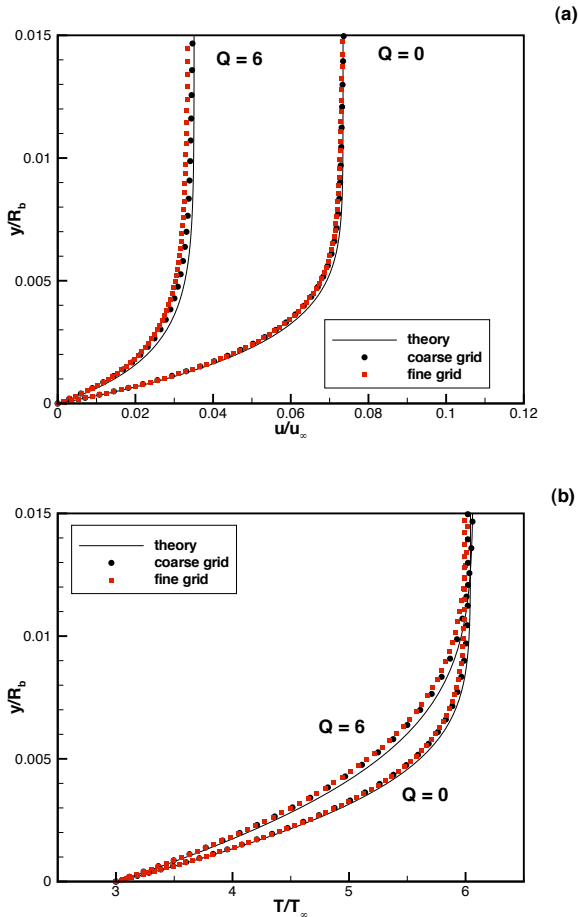
(a)

(b)

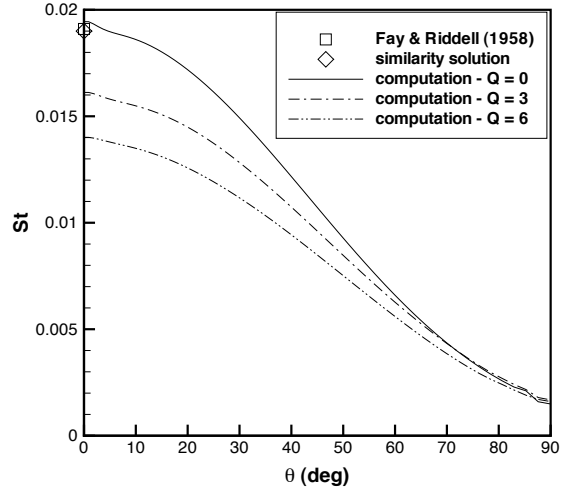Fig. 8　Boundary layer profiles, $\theta = 6.6°$.

Fig. 9　Effect of applied magnetic field on surface heat transfer profile.
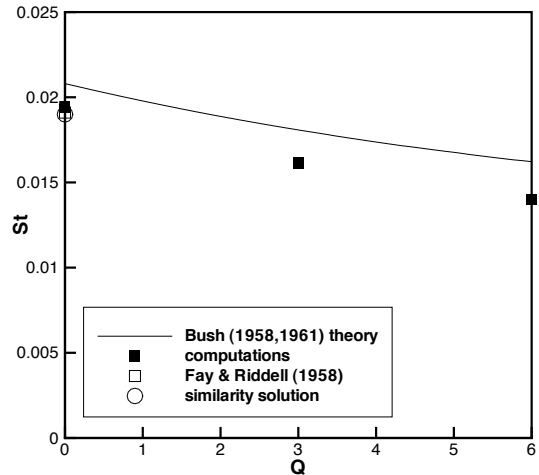
Fig. 10　Effect of applied magnetic field on stagnation point heat transfer.

dicate the predictions of Bush's similarity solution [25], with the edge conditions from the inviscid, numerical solution used as input for the similarity solution. Excellent overall agreement is obtained between theory and computation, and it is evident that results of the computations are practically mesh-independent. With the application of a strong magnetic field, the magnetic force effectively counteracts the favorable pressure gradient, decelerating the freestream and strongly reducing the velocity gradient at the wall. A similar trend is seen with the temperature profiles. The applied magnetic field causes a reduction in the temperature gradient at the wall, with a corresponding reduction in the wall heat flux.

Figure 9 shows the computed Stanton number profile around the body surface. The lines indicate the computational results (coarse grid) for different values of the interaction parameter, whereas the symbols indicate the stagnation point value computed using the Fay-Riddell [27] correlation and using a similarity solution of the non-magnetic boundary layer equations. An applied magnetic field is seen, in the computations, to reduce the level of heat transfer over the major portion of the hemisphere, with the greatest reductions in the vicinity of the stagnation point ($\theta = 0°$). The heat transfer does not change near $\theta = 90°$ because the velocity vector and magnetic field vector are nearly collinear in that part of the flow.

Figure 10 shows the Stanton number at the stagnation point as a function of the interaction parameter. The solid line represents the predictions of the combined constant density and boundary layer theories of Bush, the filled symbols are the results of the coarse-grid computations, and the open symbols represent the Fay-Riddell correlation and corresponding similarity solution. In the non-magnetic case, the computations are in good agreement with the latter heat transfer theories, whereas the prediction of Bush's theory is somewhat higher. Both theory and numerical computation predict a significant decrease in the heat transfer rate with increasing strength of the applied field, and there is good agreement between the two models in the fractional change in heat transfer. The overall higher value predicted by Bush's theory is probably due to an overestimate of the velocity gradient at the boundary layer edge.

An applied magnetic field is seen, in principle, to re-

duce the stagnation point heat flux. Additional work is needed to evaluate the Hall effect (e.g., see Ref. [28]).

SHEATHS

Local flow control techniques will typically be strongly influenced by the plasma sheaths that form near electrode surfaces. A distinguishing feature of plasma sheaths is the presence of significant charge separation, which must be included in realistic modeling of these flows [13,15]. Here we consider a fluid model of supersonic, ionized gas flow over an electrode, with a drift-diffusion model of ion motion, and the application of Gauss's law to account for the effects of charge separation. The conservation of mass, momentum, and energy for the overall gas is expressed as:

$$\frac{\partial \rho}{\partial t} + \nabla \cdot (\rho \mathbf{u}) = 0, \qquad (5)$$

$$\frac{\partial}{\partial t}(\rho \mathbf{u}) + \nabla \cdot (\rho \mathbf{u}\mathbf{u} - \Sigma) = \zeta \mathbf{E}, \qquad (6)$$

$$\frac{\partial \mathcal{E}}{\partial t} + \nabla \cdot (\mathbf{u}\mathcal{E} - \Sigma \cdot \mathbf{u} + \mathbf{Q}) = \mathbf{E} \cdot \mathbf{j}, \qquad (7)$$

where $\mathcal{E} = \rho(\epsilon + u^2/2)$ is the total fluid energy per unit mass, $\Sigma_{ij} = -p\delta_{ij} + \tau_{ij}$ is the total stress tensor, $\mathbf{Q}$ is the heat flux, the net charge is ζ, and the current density is $\mathbf{j}$. The electrical quantities are determined from Maxwell's equations:

$$\nabla \cdot \mathbf{E} = \zeta/\epsilon_0, \qquad (8)$$
$$\nabla \times \mathbf{E} = 0, \qquad (9)$$

which lead to a Poisson equation for the potential. The equations for particle conservation and momentum conservation for the ions are:

$$\frac{\partial n_i}{\partial t} + \nabla \cdot (n_i \mathbf{u} + \Gamma_i) = 0, \qquad (10)$$

$$\Gamma_i = n_i \mu_i \mathbf{E} - D_i \nabla n_i. \qquad (11)$$

The electrons are taken to be in Boltzmann equilibrium: $n_e = n_\infty \exp(e\Phi/k_B T_e)$, where the electron temperature T_e is constant, and the potential is referenced to the uniform freestream flow.

A preliminary study of a supersonic argon gas flow over a 30 mm diameter cylindrical cathode is presented here. The freestream Mach number was 3, the Reynolds number based on cylinder diameter was $\mathrm{Re}_D = 1140$, and an adiabatic, no-slip wall boundary condition was assumed. The cylinder was maintained at a potential of $\phi_w = -50$ V relative to the freestream. The freestream conditions for the neutral gas were $p_\infty = 22$ Pa and $T_\infty = 247$ K, the electron temperature was $T_e = 11600$ K (1 eV), and the fractional ionization was 10^{-8}. These conditions were chosen to roughly match those that can be obtained in laboratory wind tunnels. A computational grid of 61×101 points was used, distributed over the upper half plane.

The computed pressure field is shown in Fig. 11, where the flow is from left to right and the contour interval is 20 Pa. As expected with such a low level of ionization, the pressure field in the present ionized gas case was
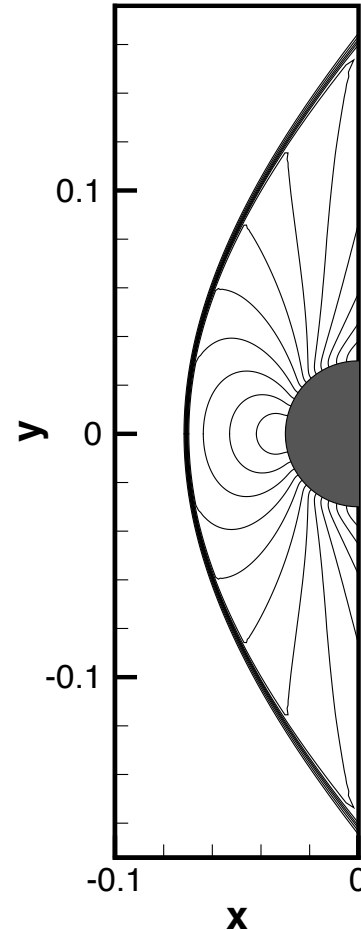

Fig. 11 Computed pressure field for Mach 3 argon flow over a cylinder.

found to be essentially identical to that obtained in the corresponding neutral gas case (not shown). The bow shock is evident as the sharp pressure gradient upstream of the cylinder. Near the symmetry plane, the flow between the shock and the body surface is subsonic. A change in the character of the pressure field is evident as the flow accelerates to supersonic speed around the shoulder of the body. Approaching the body from the shock, the effect of the viscous boundary layer is evident as a realignment of the pressure contours toward the radial direction.

The corresponding potential distribution is shown in Fig. 12. The contour interval is 5 V in this figure, and only a portion of the domain near the cylinder is shown. The potential varies only in a thin layer near the body (electrode) surface; this layer corresponds to the plasma sheath. The sheath thickness is seen to grow around the circumference of the cylinder in the same manner as that of the fluid dynamic boundary layer.

Figure 13 shows profiles of the relevant flow variables along the stagnation streamline. There is an initial jump in the number densities, pressure, and temperature, and a concomitant drop in velocity, due to the presence of the bow shock. Downstream of the shock, the fluid dynamic variables show a gradual change due to flow deceleration along the stagnation streamline. Closer to the cylinder
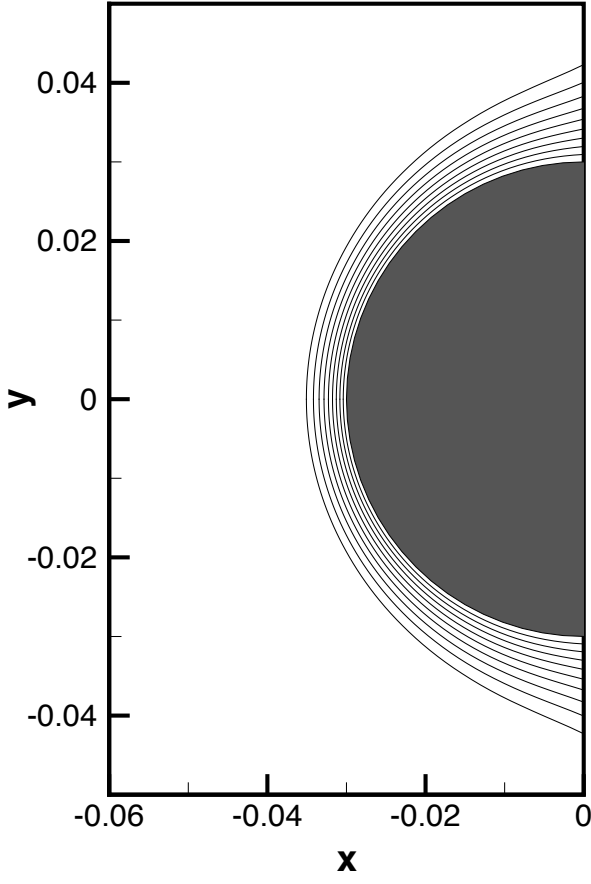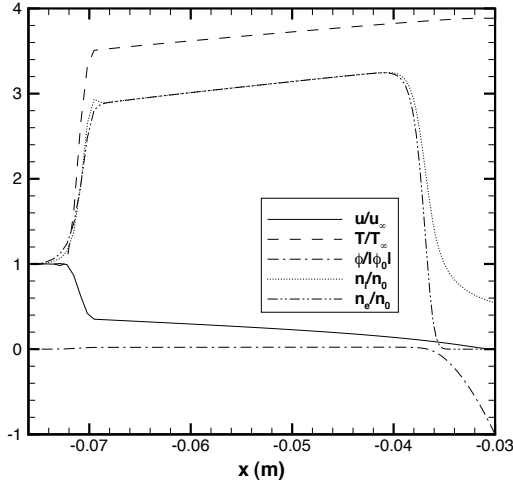
Fig. 12 Computed potential distribution.

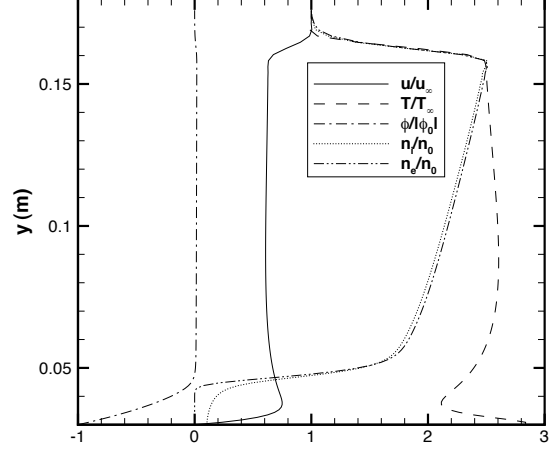**Fig. 13 Profiles along centerline.**

Fig. 14 Profiles along outlet plane.

surface, there is a sudden drop in the potential and a corresponding charge separation indicating the presence of the plasma sheath.

A similar pattern is seen at the outlet plane, Fig. 14. Note that the dependent variables are plotted on the horizontal axis in this plot, and the independent variable (y) is shown on the vertical axis, corresponding to its position in Fig. 11. The bow shock is represented by the sudden jump in the variables at the top of the figure, and the behavior closer to the cylinder corresponds to a viscous shock layer flow. Again, the plasma sheath manifests itself as a potential drop and charge separation near the electrode surface.

MAGNETOHYDRODYNAMIC BYPASS

Computations of the magnetohydrodynamic bypass concept were based on a magnetohydrodynamic, single fluid model in the low magnetic Reynolds number regime [14]. The conservation of mass, momentum, and energy is expressed as:

$$\frac{\partial \rho}{\partial t} + \nabla \cdot (\rho \mathbf{u}) \;=\; 0, \tag{12}$$

$$\frac{\partial}{\partial t}(\rho \mathbf{u}) + \nabla \cdot (\rho \mathbf{u}\mathbf{u} - \mathbf{\Sigma}) \;=\; \mathbf{j} \times \mathbf{B}, \tag{13}$$

$$\frac{\partial \mathcal{E}}{\partial t} + \nabla \cdot (\mathbf{u}\mathcal{E} - \mathbf{\Sigma} \cdot \mathbf{u} + \mathbf{Q}) \;=\; \mathbf{E} \cdot \mathbf{j}, \tag{14}$$

where $\mathcal{E} = \rho(\epsilon + u^2/2)$ is the total fluid energy per unit mass, $\Sigma_{ij} = -p\delta_{ij} + \tau_{ij}$ is the total stress tensor, and $\mathbf{Q}$ is the heat flux. The electrical quantities are determined from Maxwell's equations:

$$\nabla \cdot \mathbf{B} \;=\; 0, \tag{15}$$
$$\nabla \times \mathbf{B} \;=\; 0, \tag{16}$$
$$\nabla \cdot \mathbf{j} \;=\; 0, \tag{17}$$
$$\nabla \times \mathbf{E} \;=\; 0, \tag{18}$$

combined with the generalized Ohm's law:

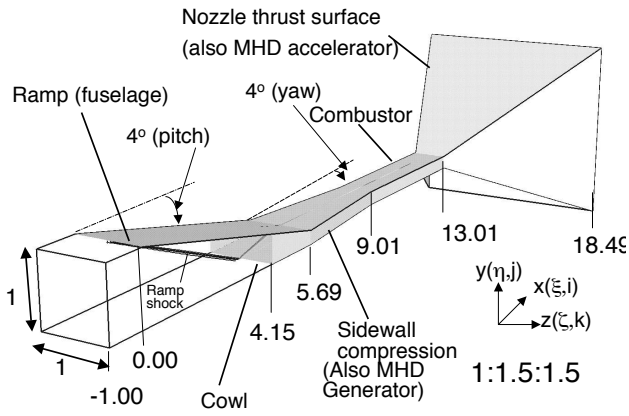$$\mathbf{j} = \sigma \cdot [\mathbf{E} + \mathbf{u} \times \mathbf{B}]. \tag{19}$$

Fig. 15 Non-dimensional distances and coordinate orientation of scramjet flowpath configuration.
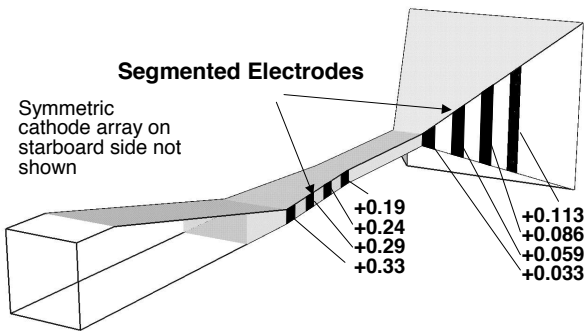

Fig. 16 Segmented electrode configuration for simulated scramjet.

Fig. 17 Three-dimensional flow separation in the absence of magnetohydrodynamic effects.

The current continuity equation must be solved for the electric field simultaneously with the fluid equations. The magnetic field can be found in advance from the solution of a Laplace equation.

The magnetohydrodynamic bypass concept was explored by computing the three-dimensional flow field through a simplified scramjet device (Fig. 15). The inlet utilizes a dual-plane compression concept. The pitch-plane shock from the ramp ($4°$ angle) reflects off the cowl lip. Sidewalls start at the cowl lip station. The fuselage ramp terminates at the point where the shock reflected from the cowl lip intersects the upper wall. At this point, sidewalls are converged at $4°$ inclination each, to obtain spanwise compressions. Sidewall compressions terminate where these crossing shocks reach the opposite walls. At this point, a constant-area duct is introduced to serve as an isolator and combustor, which is followed by a nozzle with $15°$ thrust surfaces. The freestream flow parameters are assumed to be $M = 8$, $T_\infty = 250$ K, $Re = 1.6 \times 10^6$ (based on width of configuration at the inlet, which is set at 0.6 m).

To explore magnetohydrodynamic effects, four segmented-electrode pairs were placed in the generator and the accelerator respectively, as depicted in Fig. 16. The generator segment was placed in the horizontal diffuser part of the configuration while the accelerator was placed in the nozzle, downstream of the combustor.

The fluid dynamic aspects of the scramjet flowfield are qualitatively similar for both the baseline and mag-
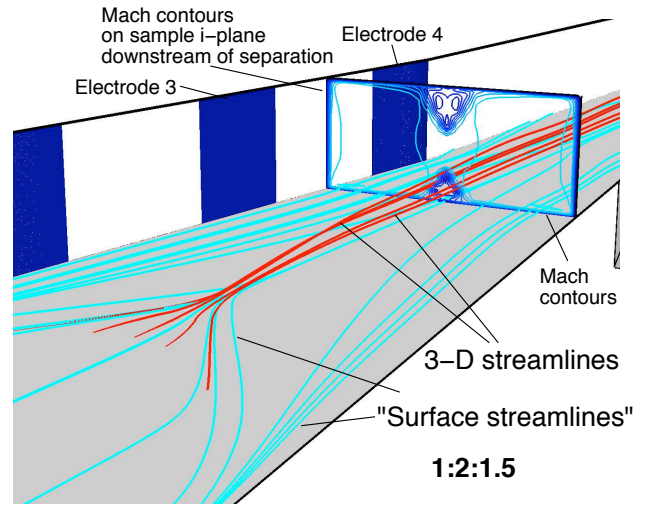
netohydrodynamic bypass cases. We describe first the baseline flow in the absence of magnetohydrodynamic effects. Despite the relatively mild angles, the interaction of shocks in the horizontal diffuser with boundary layers on the upper and lower walls gives rise to three-dimensional boundary layer separation. The effect of the separation is shown in Fig. 17, which shows a three-dimensional perspective of limiting surface streamlines, selected three-dimensional stream traces and Mach contours in a plane downstream of separation. Although no magnetohydrodynamic control is applied here, the segmented electrodes (cathodes) are shown in this figure to provide a reference point with respect to Fig. 16. A line of coalescence, indicative of flow separation, is evident in the limiting streamlines of the lower wall. A line of divergence (or attachment) is also observed near the sidewalls. The pattern is similar to that observed in the turbulent double fin interaction [29]. The three-dimensional streamlines are seen to lift off from the lower wall (the equivalent effect from the upper wall has not been shown for the purpose of clarity). The ejection of lower speed fluid from near the wall is manifested as two arch-like regions of lower Mach number (and velocity) at the center of the channel. The upper region is larger than the lower region, and reflects the fact that the upper wall boundary layer has a different history because of the asymmetry inherent in the vertical diffuser section. Note that although separation is evident, there is *no* significant region of *reversed flow*. This observation highlights the fundamentally three-dimensional nature of the interaction.

With the operation of the magnetohydrodynamic bypass system, a complicated, three-dimensional pattern of current flow appears in the scramjet device. Current lines established in the generator are depicted in Fig. 18. The current is opposed to the electric field; the dominant term in Ohm's law is $\vec{U} \times \vec{B}$ here. At the upstream electrodes, most of the current flows in the center of the channel, and the magnitude decays near the upper and lower walls, where the conductivity diminishes. Although electrical conductivity also decreases
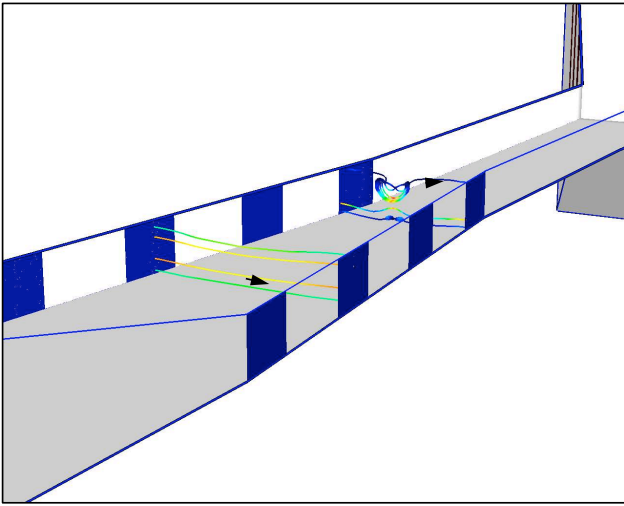
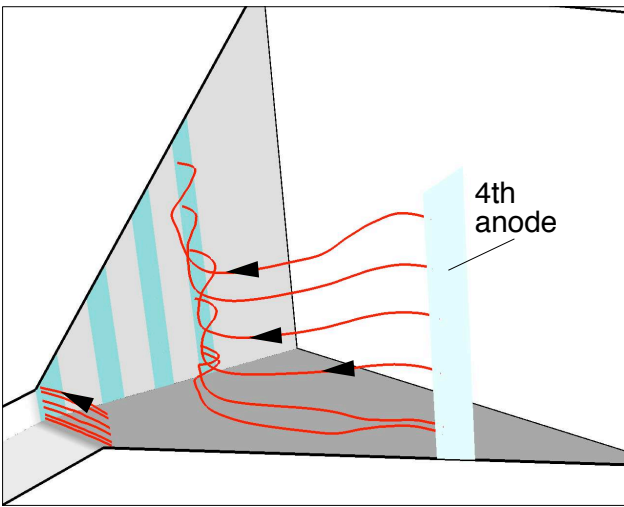**Fig. 18   Selected current lines in the generator.**

Fig. 19   Selected current lines in the accelerator.

near the electrodes, no reduction in current is observed because the decrease in σ is compensated by corresponding changes in electric and velocity fields to satisfy the constraint of current continuity. The current field near the trailing edge of the generator is considerably more complex. A spirally wound current path is observed, and is correlated with the separation regions of low Mach number. The net result is a region of reversed current relative to the bulk, even though the streamwise velocity is always positive. The phenomenon is consistent with the fact that the electric field is relatively uniform and, in regions of low velocity, overcomes the motional *emf* to yield locally reversed current.

A corresponding set of current lines for the accelerator are shown in Fig. 19. Note that in this three-dimensional perspective view, only one anode is depicted for clarity. Here the current is in the direction of the imposed electric field. Due to numerical difficulties, only a small value of the interaction parameter was used for the accelerator. The current is relatively uniform at the entrance to the nozzle and magnitudes are much lower than in the generator, because of the small imposed interaction parameter. At the downstream section, however, the current paths are considerably curved and inclined up-
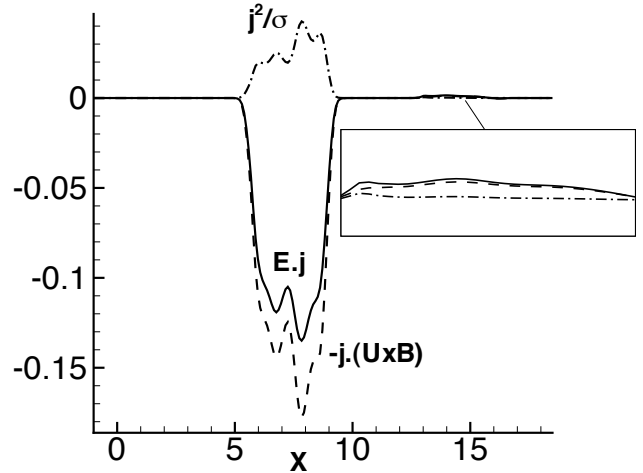

Fig. 20   Energy interactions along centerline of channel

stream. Since the electric field is relatively uniform, this is primarily the effect of the velocity field, which flares outward as it expands in the nozzle.

Another aspect of the scramjet flow explored in this preliminary analysis concerns the energy interactions between the magnetic and fluid fields. Figure 20 shows the total term in the energy equation, $\vec{E} \cdot \vec{j}$, and its two components, the work interaction, $-\vec{j} \cdot \left(\vec{U} \times \vec{B} \right)$ and the Joule heating term, $\vec{j} \cdot \vec{j}/\sigma$ along the centerline. The major interaction occurs in the generator because of the higher interaction parameter. The total term is negative here, because the extraction of energy from the mean flow is significantly higher than the Joule heating term and indicates a relatively efficient procedure. In the accelerator, both components of $\vec{E} \cdot \vec{j}$ are positive since here the current and $\vec{U} \times \vec{B}$ are generally opposed. Note however that the Joule heating is the smaller component of the total value. This promising observation must be reevaluated for more realistic conditions in which the interaction parameter is increased, and turbulence and Hall effects are included.

CONCLUSIONS

Over the last few years, the international hypersonics research community has been exploring the possibilities of plasma-based flow control. In support of this effort, the Computational Sciences Center at the United States Air Force Research Laboratory (AFRL/VAAC) has developed a set of computational tools to examine some of the proposed electromagnetic flow control techniques. Several applications have been studied, and the results are summarized in the present paper.

The first application examined involved the possibility of shock wave mitigation with non-equilibrium ionization introduced upstream. A careful analysis of experiments on shock propagation through a glow discharge showed that a nonuniform upstream temperature field is the primary cause of the changes in the behavior of the shock. The possibility exists that ionization may directly affect the shock behavior under different conditions, but future

studies must use extreme care to rule out thermal effects in order to prove this. Since there are few effective ways to deliver thermal energy to a hypersonic flow, due to extremely short particle residence times in any flow control device, thermal energy addition by plasma methods may be a technology of interest in hypersonic applications.

A second application examined was stagnation point heat transfer mitigation using magnetic deceleration. A significant reduction in stagnation point heat transfer was observed in computations, and this appears to be a promising technology for atmospheric entry applications, in which significant thermal ionization is present between the bow shock and the stagnation point. Ongoing work is addressing the issue of the Hall effect in this application.

Although significant ionization and electric conductivity can be expected at the extremely high Mach numbers of reentry flight, a method for augmenting the electric conductivity (such as electron beam ionization) will be necessary for applications to a lower speed regime. In order to make the requirements for power and added weight for such augmentation reasonable, plasma-based control schemes will probably have to be limited to relatively small regions. A local control scheme of particular interest involves introducing a thin sheet of ionization at a solid surface in order to manipulate the heat flux and skin friction. In such control schemes plasma sheaths will have a dominant effect; we have made some preliminary calculations of their interaction with a supersonic crossflow.

Finally, the magnetohydrodynamic bypass concept for scramjet engines was explored. This is a long-term research effort because of the complexity of both the scramjet device and conductivity augmentation methods. Nevertheless, promising results have been obtained for a simplified, three-dimensional scramjet configuration, and ongoing efforts will increase the physical fidelity of the modeling of this device.

ACKNOWLEDGMENTS

REFERENCES

[1]Rossow, V. J., "On Flow of Electrically Conducting Fluids Over a Flat Plate in the Presence of a Transverse Magnetic Field," NACA Report 1358, National Advisory Committee for Aeronautics, Washington, DC, March 1957.

[2]Ziemer, R. W. and Bush, W. B., "Magnetic Field Effects on Bow Shock Stand-off Distance," Physical Review Letters, Vol. 1, No. 2, 1958, pp. 58–59.

[3]Gurijanov, E. P. and Harsha, P. T., "AJAX: New Directions in Hypersonic Technology," AIAA Paper 96-4609, November 1996.

[4]Poggie, J., "Modeling the Effects of Weak Ionization on Supersonic Flow and Shock Waves," AIAA Paper 99-0867, January 1999.

[5]Gaitonde, D. V., "Development of a Solver for 3-D Non-Ideal Magnetogasdynamics," AIAA Paper 99-3610, June 1999.

[6]Poggie, J., "Energy Addition for Shockwave Control," AIAA Paper 99-3612, June 1999.

[7]Poggie, J., "Modeling the Propagation of a Shock Wave through a Glow Discharge," AIAA Journal, Vol. 38, No. 8, August 2000, pp. 1411–1418.

[8]Poggie, J. and Gaitonde, D. V., "Magnetic Control of Hypersonic Blunt Body Flow," AIAA Paper 2000-0452, January 2000.

[9]Gaitonde, D. V. and Poggie, J., "Simulation of MHD Flow Control Techniques," AIAA Paper 2000-2326, June 2000.

[10]Poggie, J. and Gaitonde, D. V., "Computational Studies of Magnetic Control in Hypersonic Flow," AIAA Paper 2001-0196, January 2001.

[11]Gaitonde, D. V. and Poggie, J., "An Implicit Technique for 3-D Turbulent MGD with the Generalized Ohm's Law," AIAA Paper 2001-2736, June 2001.

[12]Gaitonde, D. V. and Poggie, J., "Elements of a Numerical Procedure for 3-D MGD Flow Control Analysis," AIAA Paper 2002-0198, January 2002.

[13]Poggie, J. and Gaitonde, D. V., "Electrode Boundary Conditions in Magnetogasdynamic Flow Control," AIAA Paper 2002-0199, January 2002.

[14]Gaitonde, D. V. and Poggie, J., "Preliminary Analysis of 3-D Scramjet Flowpath with MGD Control," AIAA Paper 2002-2134, May 2002.

[15]Poggie, J., Gaitonde, D. V., and Sternberg, N., "Numerical Simulation of Plasma Sheaths in Aerodynamic Applications," AIAA Paper 2002-2166, May 2002.

[16]Poggie, J. and Gaitonde, D. V., "Magnetic Control of Flow Past a Blunt Body: Numerical Validation and Exploration," Physics of Fluids, Vol. 14, No. 5, 2002, pp. 1720–1731.

[17]Klimov, A. I., Koblov, A. N., Mishin, G. I., Serov, Y. L., and Yavor, I. P., "Shock Wave Propagation in a Glow Discharge," Soviet Technical Physics Letters, Vol. 8, No. 4, 1982, pp. 192–194.

[18]Ganguly, B. N., Bletzinger, P., and Garscadden, A., "Shock Wave Damping and Dispersion in Nonequilibrium Low Pressure Argon Plasmas," Physics Letters A, Vol. 230, 1997, pp. 218–222.

[19]Voinovich, P. A., Ershov, A. P., Ponomareva, S. E., and Shibkov, V. M., "Propagation of Weak Shock Waves in Plasma of Longitudinal Flow Discharge in Air," High Temperature, Vol. 29, No. 3, 1991, pp. 468–476.

[20]Hilbun, W. M., Shock Waves in Nonequilibrium Gases and Plasmas, Ph.D. thesis, Air Force Institute of Technology, Wright-Patterson AFB, OH, October 1997.

[21]Ford, C. A. and Glass, I. I., "An Experimental Study of One-Dimensional Shock-Wave Refraction," Journal of the Aeronautical Sciences, Vol. 23, No. 2, 1956, pp. 189–191.

[22]Macheret, S. O., Ionikh, Y. Z., Chernysheva, N. V., Yalin, A. P., Martinelli, L., and Miles, R. B., "Shock Wave Propagation and Dispersion in Glow Discharge Plasmas," Physics of Fluids, Vol. 13, No. 9, 2001, pp. 2693–2703.

[23]Bush, W. B., "Magnetohydrodynamic-Hypersonic Flow Past a Blunt Body," Journal of the Aero/Space Sciences, Vol. 25, No. 11, 1958, pp. 685–690,728.

[24]Coakley, J. F. and Porter, R. W., "Time-Dependent Numerical Analysis of MHD Blunt Body Problem," AIAA Journal, Vol. 9, No. 8, 1971, pp. 1624–1626.

[25]Bush, W. B., "The Stagnation-Point Boundary Layer in the Presence of an Applied Magnetic Field," Journal of the Aerospace Sciences, Vol. 28, No. 8, 1961, pp. 610–611,630.

[26]Ambrosio, A. and Wortman, A., "Stagnation Point Shock Detachment Distance for Flow Around Spheres and Cylinders," ARS Journal, Vol. 32, No. 2, 1962, pp. 281.

[27]Fay, J. A. and Riddell, F. R., "Theory of Stagnation Point Heat Transfer in Dissociated Air," Journal of the Aeronautical Sciences, Vol. 25, No. 2, 1958, pp. 73–85,121.

[28]Porter, R. W. and Cambel, A. B., "Hall Effect in Flight Magnetogasdynamics," AIAA Journal, Vol. 5, No. 12, 1967, pp. 2208–2213.

[29]Gaitonde, D. and Shang, J. S., "The Structure of a Double-Fin Turbulent Interaction at Mach 4," AIAA Journal, Vol. 33, No. 12, 1995, pp. 2250–2258.